Glutathione-Responsive Self-Assembled Magnetic Gold Nanowreath for Enhanced Tumor Imaging and Imaging-Guided Photothermal Therapy

Yijing Liu,[†] Zhen Yang,[†] Xiaolin Huang,[†,‖] Guocan Yu,[†] Sheng Wang,[†] Zijian Zhou,[†] Zheyu Shen,*[,†,§] Wenpei Fan,[†] Yi Liu,[‡,#] Matthew Davisson,[⊥] Heather Kalish,[⊥] Gang Niu,[†] Zhihong Nie,*[,‡] and Xiaoyuan Chen*[,†]

[†]Laboratory of Molecular Imaging and Nanomedicine, National Institute of Biomedical Imaging and Bioengineering, National Institutes of Health, Bethesda, Maryland 20892, United States

[‡]Department of Chemistry and Biochemistry, University of Maryland, College Park, Maryland 20742, United States

[§]CAS Key Laboratory of Magnetic Materials and Devices, Key Laboratory of Additive Manufacturing Materials of Zhejiang Province, and Division of Functional Materials and Nanodevices, Ningbo Institute of Materials Technology and Engineering, Chinese Academy of Sciences, 1219 Zhongguan West Road, Ningbo, Zhejiang 315201, China

[‖]State Key Laboratory of Food Science and Technology, Nanchang University, Nanchang 330047, P. R. China

[⊥]Trans-NIH Shared Resource on Biomedical Engineering and Physical Science, Institute of Biomedical Imaging and Bioengineering, National Institutes of Health, Bethesda, Maryland 20892, United States

[#]State Key Laboratory of Supramolecular Structure and Materials, College of Chemistry, Jilin University, Changchun 130012, P. R. China

Ⓢ *Supporting Information*
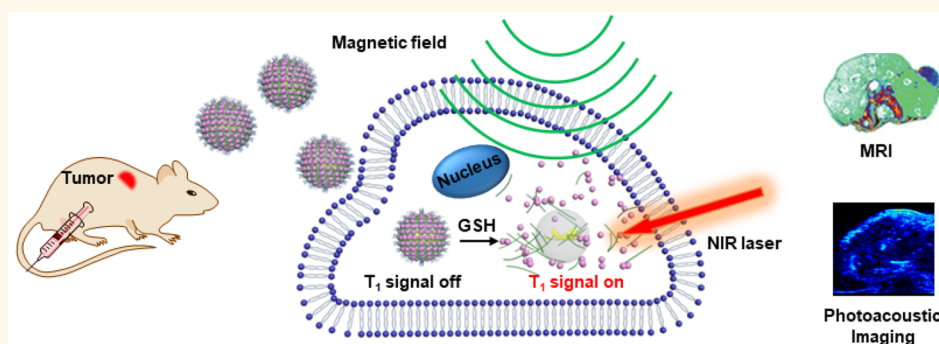
ABSTRACT: Designing nanomaterials with advanced functions and physical properties to improve cancer diagnosis and treatment has been an enormous challenge. In this work, we report the synthesis of magnetic gold nanowreaths (AuNWs) by combining wet-chemical synthesis with layer-by-layer self-assembly. The presence of Au branches, small junctions, and central holes in AuNWs led to improved photothermal effect compared with Au nanoring seeds and thick Au nanoring with smooth surface. The self-assembly of exceedingly small magnetic iron oxide nanoparticles (ES-MIONs) on the surfaces of AuNWs not only effectively quenched the T_1-weighted magnetic resonance imaging (MRI) ability due to the enhanced T_2 decaying effect but also provided the responsiveness to glutathione (GSH). After intravenous injection, the T_1 signal of magnetic AuNWs initially in the "OFF" state can be intelligently switched on in response to the relatively high GSH concentration in tumor, and the formation of larger assemblies of ES-MIONs improved their tumor delivery compared to ES-MIONs themselves. Thus, the magnetic AuNWs showed higher MRI contrast than ES-MIONs or commercial Magnevist in T_1-weighted MR imaging of tumor. Furthermore, the magnetic AuNWs have absorption in near-infrared

continued...

range, leading to strong photoacoustic signal and effective photoablation of tumor. Therefore, our GSH-responsive self-assembled magnetic AuNWs could enhance T_1-weighted MRI and photoacoustic imaging of tumor and be used for imaging-guided photothermal therapy.

Inorganic nanomaterials have shown great potential in improving diagnosis and treatment outcomes of cancers due to their physical properties and enhanced tumor accumulation through the enhanced permeability and retention (EPR) effect and active targeting.[1-4] Recent advances in material fabrication via wet-chemical synthesis, self-assembly, and so on, have continuously improved the physical properties of nanomaterials.[5-10] To meet the rising demand for materials with advanced functions, more hierarchical and stimuli-responsive nanostructures are desired, which would be challenging to prepare through a single synthesis strategy. The combination of different synthesis techniques could further increase the structural complexity and functional diversity of nanomaterials for advanced applications.[11,12] Besides structures and functions, the effectiveness of nano diagnostic and therapeutic agents in many *in vivo* biomedical applications is insufficient due to their low tumor delivery efficiency.[13,14] Whether the tumor delivery efficiency of nanoparticles can be improved or not is determined by their capability to overcome the biological barriers *in vivo*, which is closely related to their own physical properties, such as size and stimuli-responsiveness.[15-19] Therefore, nanomaterials with improved

therapeutic and diagnostic functions as well as suitable physical properties should be developed.

Among various inorganic nanomaterials, gold (Au) nanomaterials, have been extensively applied in diverse biomedical applications, which include photoacoustic imaging and photothermal ablation of tumors, due to their optical and photothermal properties.[20-23] In most cases, Au nanomaterials with near-infrared (NIR) absorption were used. The success of treatment is strongly associated with the photothermal efficiency of the Au nanomaterials and determination of the best time window for conducting therapy via various imaging techniques.[24,25] Superparamagnetic iron oxide nanoparticles (SPION) have been applied as contrast agents to enhance T_2-weighted magnetic resonance imaging (MRI).[26] However, most of the commercial T_2 contrast agents based on SPION have been removed from the market because physicians prefer to use T_1 contrast agents.[27,28] Subsequently, exceedingly small magnetic iron oxide nanoparticles (ES-MIONs) (<5 nm) were developed as T_1-weighted MRI contrast agents. The ES-MIONs have attracted intense research interest because they are more biocompatible than gadolinium chelates, which occupied most of the MRI contrast agent market.[27,29-31] However, their fast renal clearance
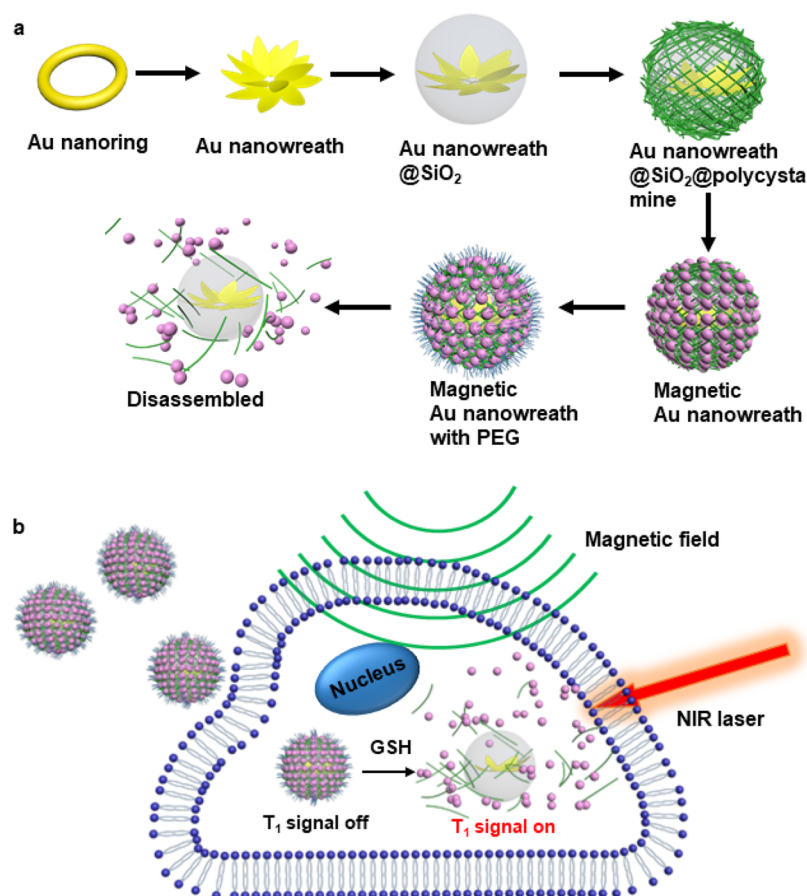

Figure 1. Schematic illustration of the synthesis of magnetic gold nanowreath and their applications as GSH-responsive T_1-weighted imaging contrast agents and photothermal agents.
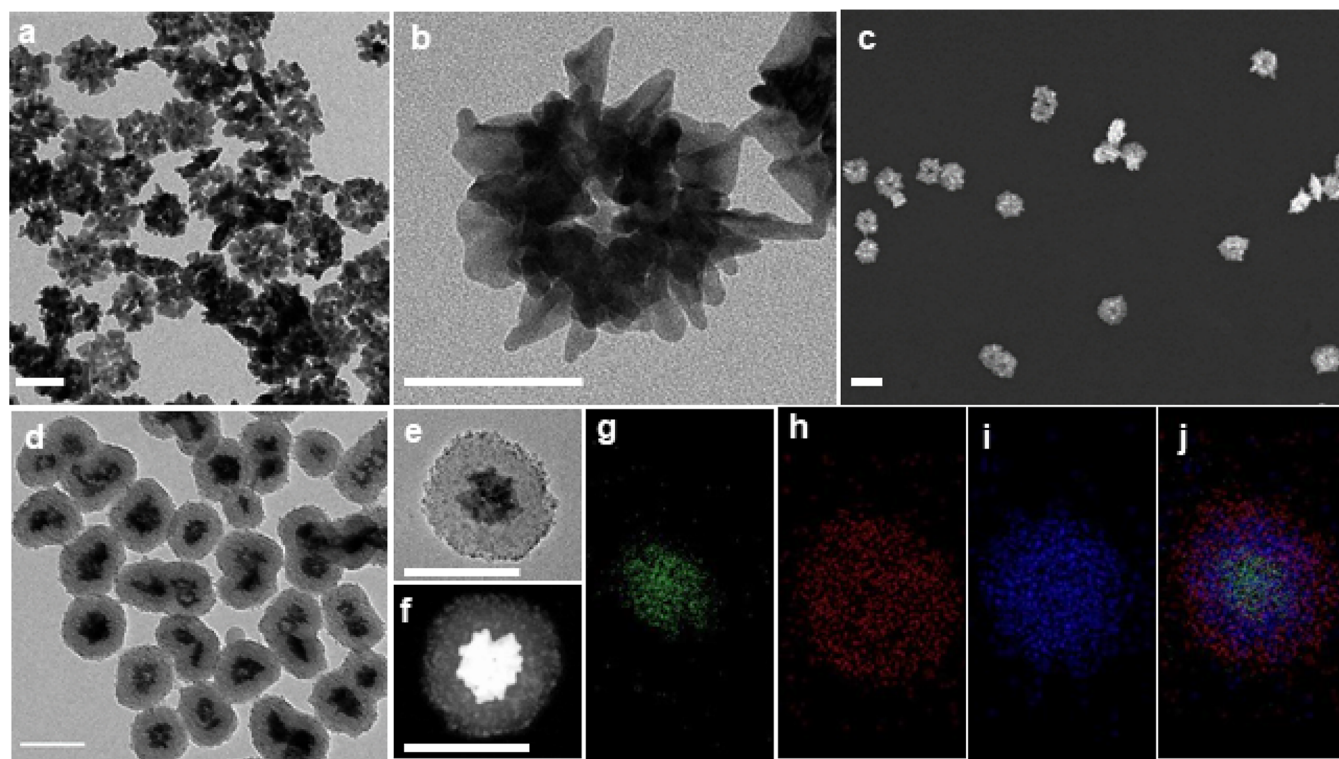
Figure 2. Representative TEM and SEM images of AuNWs and magnetic AuNWs. (a,b) Representative TEM images and (c) SEM image of AuNWs. (d,e) Representative TEM images and (f) high-annular dark-field TEM image of magnetic AuNWs. (g–j) Energy dispersive X-ray spectroscopy characterization of a magnetic AuNW indicating the presence of (g) Au, (h) Fe, and (i) Si in the nanoparticle, and (j) the distribution of three elements in the overlapped image. Scale bars: 50 nm in a–c and 100 nm in d–f.

would negatively impact their tumor accumulation and imaging ability.[28] In addition, the signal from T_1-weighted MRI could be interrupted by other tissues such as fat.[32] Combining MRI with a secondary imaging modality would be helpful to avoid such interference for more accurate tumor imaging and diagnosis.

Here we report the synthesis of glutathione (GSH)-responsive magnetic Au nanowreath (AuNW) through combination of wet-chemical synthesis and layer-by-layer self-assembly (Figure 1a). The synthesized magnetic AuNWs could turn on their T_1-weighted MRI signals by responding to GSH in tumor microenvironment, enhance contrast of photoacoustic imaging, and be used for photothermal ablation of tumors (Figure 1b).[33–38] The magnetic AuNW contains AuNW as the inner core, assembled ES-MIONs as the outside shell, and a layer of silica between core and shell. Polyethylene glycol (MW 5 K) were conjugated to the carboxyl groups on ES-MIONs. The presence of Au branches, small junctions and central holes in AuNWs can generate strong plasmon coupling within the nanostructures, leading to improved photothermal properties compared with Au nanorings. The initial magnetic AuNWs have a weak T_1 imaging ability due to the strong quenching from T_2 decaying effect. By reacting with GSH, the assembled ES-MIONs could be released from magnetic AuNWs, "turning on" the T_1 imaging function. Consequently, the longitudinal relaxivity (r_1) of magnetic AuNWs after incubation in GSH solution increased 2.8 times compared with that before incubation. Furthermore, the tumor accumulation of the magnetic AuNWs was significantly enhanced compared with that of the individual ES-MIONs, leading to 2.5 times enhancement of the T_1 imaging signal at 24 h postinjection. Finally, we demonstrated the photoacoustic imaging ability of the magnetic AuNWs for tumors and the effective removal of subcutaneous tumor model through photothermal therapy.

RESULTS AND DISCUSSION

Preparation and Characterization of Magnetic AuNWs. The AuNWs were synthesized by a seed-mediated growth method using Au nanorings as seeds. The Au nanorings were prepared via a previously reported silver (Ag)-plate-template mediated method (Supporting Information (SI), Figure S1a).[18] The initial Au nanoring template have an average diameter of 40 nm (SI, Figure S1b). Then AuNWs were prepared by growing sharp branches from the Au nanoring seeds, as indicated by the TEM and SEM images (Figure 2a–c). The average diameter of AuNW is 61.2 nm measured from TEM images. Because of the two-dimensional (2D) structure of seeds, the synthesized AuNWs were also 2D with an average thickness of 20 nm, measured from TEM and SEM images (Figure 2a–c). The length of Au branches, the diameter, and the central hole size of AuNWs can be controlled by the ratio of Au precursor to Au nanoring seeds (SI, Figure S2a–c). To generate stronger plasmonic coupling, AuNWs with relatively long Au branches and small central hole size were used in this study. In the presence of sodium citrate, thicker Au nanorings with smooth surfaces were formed (SI, Figure S 2d,e). To construct magnetic AuNWs, the silica shell was grown on the surfaces of AnNWs to provide negatively charged surfaces for the subsequent layer-by-layer assembly of positively charged polymers and negatively charged ES-MIONs, consecutively (SI, Figure S3). In the first layer-by-layer assembly, the positively charged polymers contain cystamine and oligo-(ethylene glycol) methyl ether methacrylate as repeating units (see Methods and SI, Figure S4–8, synthesis details). The disulfide bonds in polycystamine blocks can be cleaved in response to GSH. In the second step of layer-by-layer assembly, the negatively charged poly(acrylic acid)-stabilized ES-MIONs were
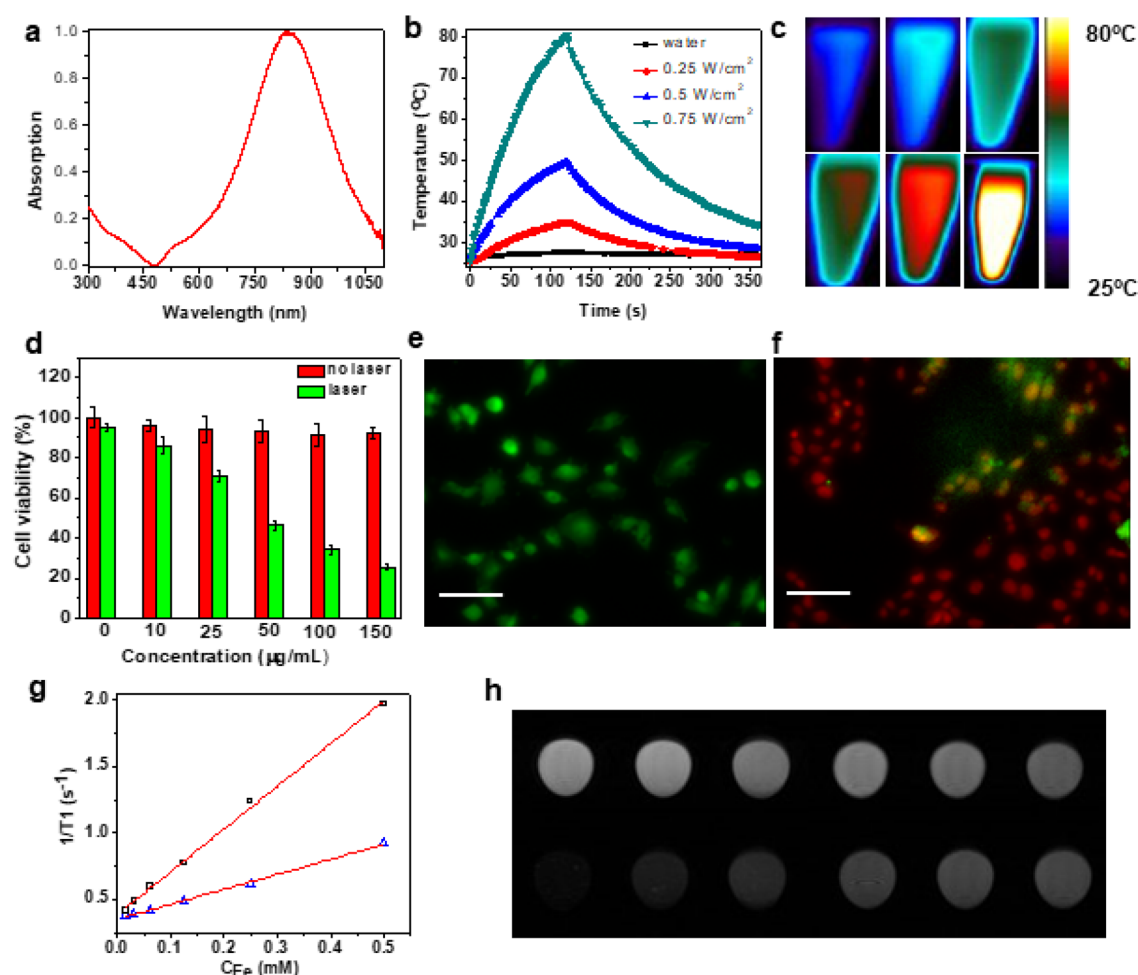
Figure 3. Photothermal and T_1-weighted MRI characterizations of magnetic AuNWs. (a) UV−vis absorption spectrum of magnetic AuNWs. (b) The temperature change of the aqueous dispersion of magnetic AuNWs and pure water under the irradiation of an 808 nm laser with different power densities. The absorption of magnetic AuNWs at 808 nm was set at 0.8. The blackline represents the temperature changing curve of water irradiated by a laser at 0.75 W/cm². (c) Representative thermal images of the aqueous dispersion of magnetic AuNWs (absorption at 808 nm was 0.8) after being exposed to a NIR laser (0.75 W/cm²) for (first row from left to right) 5, 21, 37, (second row from left to right) 47, 60, and 120 s, respectively. (d) Cell viability of U87MG incubated with different amount of magnetic AuNWs for 24 h with or without being exposed to a NIR laser. The *X*-axis represents the concentrations of Au. (e.f) Fluorescence images of (e) live (green) and (f) dead (red) U87MG cells costained by calcein, AM, and ethidium bromide after incubation of magnetic AuNWs (Au concentration: 150 µg/mL) without and with NIR laser irradiation, respectively. Scale bars: 10 µm. (g) Plots of r_1 value of disassembled (square) ($y = 3.214x + 0.384$) and assembled (triangle) magnetic AuNWs ($y = 1.127x + 0.349$) and (h) their corresponding T_1-weighted images (top, disassembled; bottom, assembled). Concentrations of Fe are 0.5, 0.25, 0.125, 0.0625, 0.03125, and 0.01563 mM (from left to right).

assembled onto the positively charged nanoparticle surfaces through electrostatic interactions, forming a compact shell outside (Figure 2d−f). The surface charge conversion during the layer-by-layer self-assembly can be monitored with a ζ potential measurement (SI, Figure S9a). The ES-MIONs with a size of 3.6 nm and a high r_1 value were prepared from a previously reported coprecipitation method (SI, Figure S10).[28] From high-annular dark-field TEM image, the bright dots of ES-MIONs can be clearly visualized (Figure 2f). The presence and distribution of Au, silicon (Si), and iron (Fe) elements in the nanoparticle were characterized by energy dispersive X-ray spectroscopy (Figure 2g−j). Finally, the amine-terminated polyethylene glycol (PEG) (MW 5 K) were conjugated to the surfaces of magnetic AuNW through EDC/NHS coupling to enhance their stability. The overall diameter of magnetic AuNW is 100.7 nm, as confirmed by TEM imaging and dynamic light scattering (Figure 2d and SI, Figure S9b).

The photothermal effect of plasmonic nanoparticles relies on the conversion of energy from light to heat through nonradiative decay.[21] The presence of Au branches, small junctions between branches, and central holes in the AuNWs enabled the magnetic AuNWs with plasmon coupling within the nanoparticles and absorption peak at about 800 nm (Figure 3a). For *in vivo* applications, light with a wavelength in the range of 600−900 nm is preferred due to the relatively deep penetration depth and low background signal.[39] The absorption peak for Au nanoring seeds is around 1000 nm. Increasing the thickness of Au nanorings shifted the absorption peak position toward 800 nm and enhanced the photothermal stability. It is, however, accompanied by a decrease in the photothermal conversion efficiency, possibly due to the stronger light scattering of thicker Au nanorings.[18] This dilemma could be solved by growing Au branches from the Au nanoring seeds to generate AuNWs with strong plasmon coupling. We characterized the photothermal properties of magnetic AuNWs by exposing their aqueous dispersion to an 808 nm continuous-wave (CW) laser with different power densities. The magnetic AuNWs demonstrated excellent
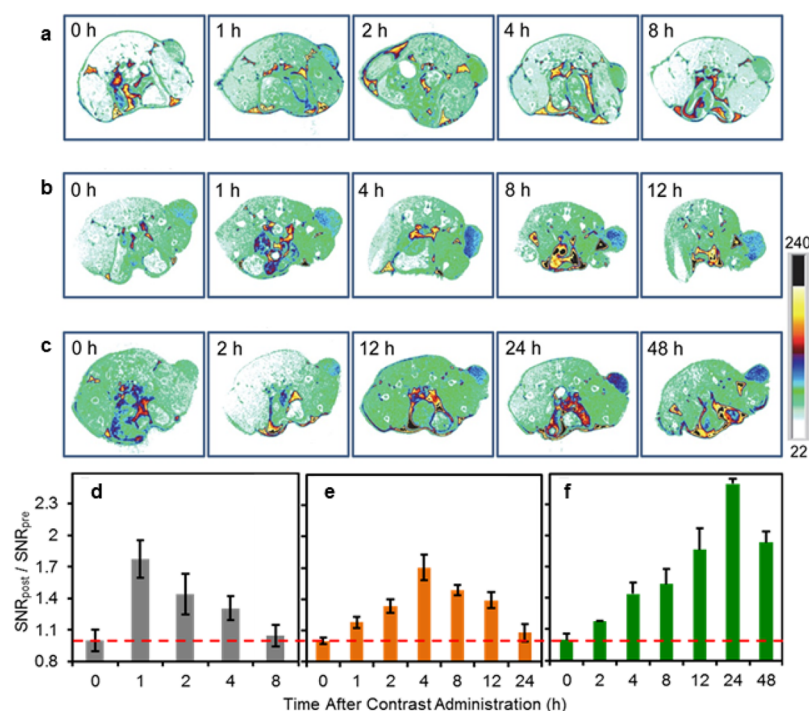
Figure 4. *In vivo* MRI of tumors. (a−c) T_1-weighted images of U87MG tumor-bearing nude mice and (d−f) corresponding quantificational analysis of the tumor signals after intravenous injection of (a,d) Magnevist (C_{Gd} = 5.0 mg/kg), (b,e) ES-MIONs (C_{Fe} = 5.0 mg/kg), and (c,f) magnetic AuNWs (C_{Fe} = 5.0 mg/kg). The MR images before injection were identified as 0 h in a−c. The signal enhancement in tumors for different contrast agents at different time points after injection were quantified as the division of signal-to-noise ratio (SNR) of tumors at different time points postinjection by the SNR of tumors at 0 h (see SI for the calcualtion of SNR).

photothermal effect, which increased the temperature of solution from 25 to 80 °C in 2 min with laser irradiation (0.75 W/cm^2) (Figure 3b,c). On the contrary, negligible temperature increase was observed when pure water was irradiated by laser at the same condition (Figure 3b). Compared with Au nanoring seeds and thick Au nanorings with smooth surfaces, the aqueous dispersion of AuNWs exhibited a higher temperature rise (SI, Figures S2a,e and S11).

We further evaluated the cytotoxicity of magnetic AuNWs and their photothermal-induced cancer cell killing ability. Different concentrations of nanoparticles were incubated with U87MG cells for 24 h in cell culture medium. Then the cell culture medium was replaced to remove nanoparticles that have not been internalized by cells. The results of MTT assay indicated relatively low cytotoxicity of the magnetic AuNWs (Figure 3d). Upon irradiation of cells with an 808 nm laser at 0.75 W/cm^2 for 10 min, significant cancer cell death was observed (Figure 3d). The cells with or without being exposed to laser irradiation were co-stained with calcein Am and ethidium bromide, followed by the observation of dead or live cells with fluorescence microscopy. Without laser irradiation, no significant cell death was observed, indicated by the high population of cells with green color (Figure 3e). With laser irradiation, effective killing of cancer cells was found by the photothermal effect of magnetic AuNWs (Figure 3f).

T_1-weighted MRI contrast agents can generate brighter signal in tumor imaging by shortening the protons' longitudinal relaxation times.[40,41] ES-MIONs with a high r_1 and low cytotoxicity are one of the excellent candidates for T_1-weighted MRI.[27] In our magnetic AuNWs, the ES-MIONs formed a compact shell outside, leading to a significantly enhanced transversal relaxivity (r_2) value due to formation of larger magnetic nanoparticle

assemblies and generation of local magnetic field inhomogeneity through magnetic coupling.[42] On the contrary, the r_1 value of ES-MIONs in magnetic AuNWs decreased due to the smaller surface-to-volume ratio of ES-MIONs in assembled state. In the absence of GSH, strong T_2 decaying in magnetic AuNWs would effectively quench the T_1 relaxation and keep the T_1 imaging function "off."[43,44] The r_1 and r_2 values of the assembled magnetic AuNWs were respectively measured to be 1.1 and 198.6 mM^{-1} s^{-1} using a 7T MRI scanner (Figure 3g and SI, Figure S12b). Because of the high r_2 value and low r_1 value and strong T_2 decaying effect, the magnetic AuNWs show darker images for both T_1-weighted and T_2-weighted images at higher concentrations (Figure 3h and SI, Figure S12a). In the presence of GSH (10 mM), the disulfide bonds in the polymers were cleaved in 2 h and the ES-MIONs were released from the magnetic AuNWs (SI, Figure S13). The release of ES-MIONs would decrease the effective size of magnetic nanoparticles and reduce local magnetic field inhomogeneity, giving rise to a decreased r_2 value of 33.9 mM^{-1} s^{-1} and an increased r_1 value of 3.2 mM^{-1} s^{-1}. As a result, the T_1 signal of the disassembled magnetic AuNWs was turned on (Figure 3g and SI, Figure S14b), leading to much brighter T_1-weighted images and T_2-weighted images (Figure 3h and SI, Figure S14a).

In Vivo MRI with Magnetic AuNWs. The T_1-weighted tumor imaging ability of our magnetic AuNWs was then evaluated using a U87MG tumor-bearing nude mice model. The ES-MIONs and commercially available Magnevist were used as controls. We first directly injected the same amount of magnetic AuNWs locally into tumor and muscle to evaluate their *in vivo* responsiveness. Both T_1-weighted MRI signals became stronger with time, indicating the successful disassembly of magnetic AuNWs *in vivo* (SI, Figure S15). The stronger T_1-weighted MRI
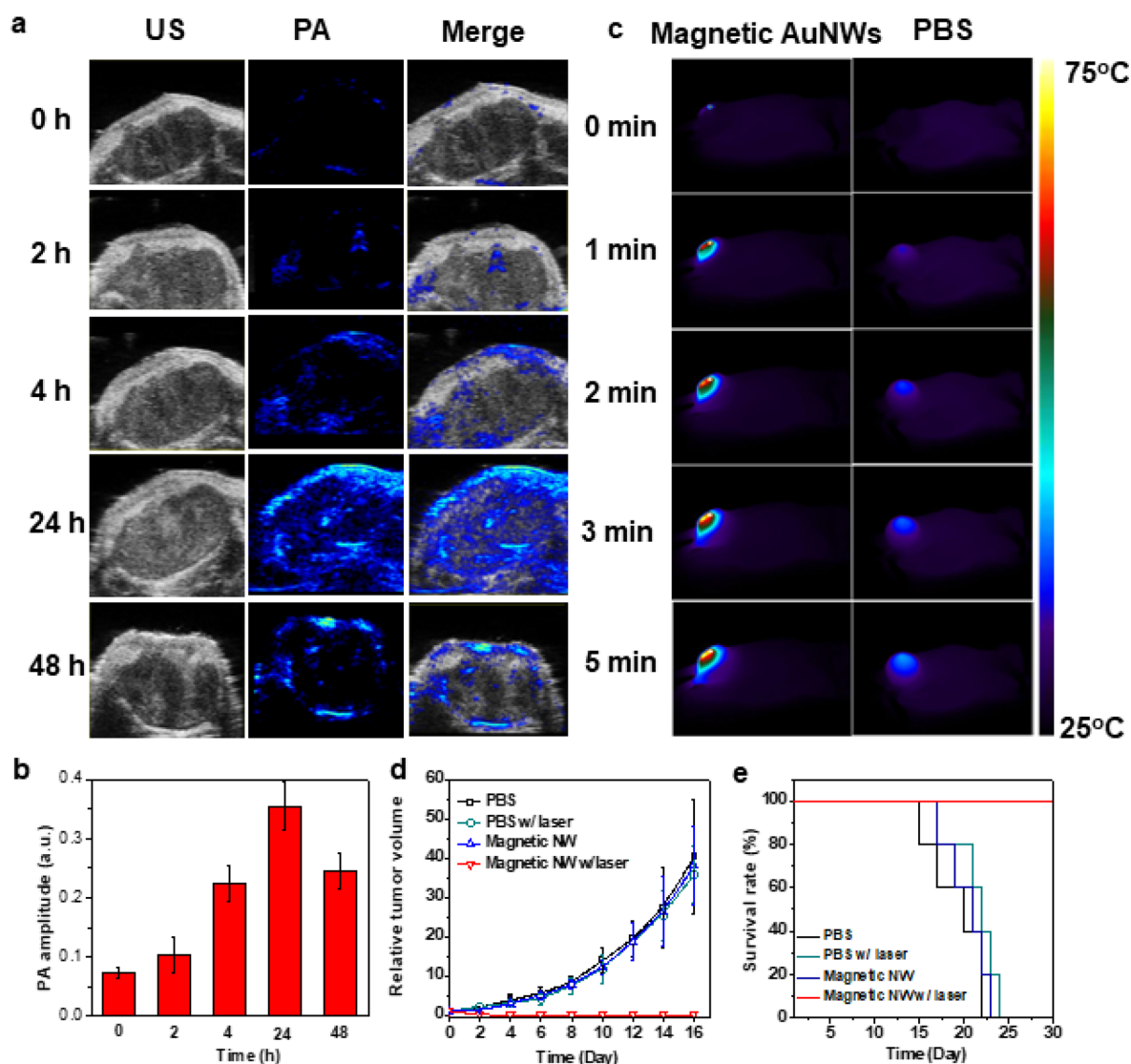
Figure 5. *In vivo* photoacoustic imaging and photothermal therapy with magnetic AuNWs. (a) Ultrasonic (US), photoacoustic imaging (PA), and merged images of tumor before injection (0 h) and at 2, 4, 24, and 48 h after intravenous injection of magnetic AuNWs upon irradiation by an 808 nm pulsed laser and (b) their corresponding quantified photoacoustic signals. (c) Representative thermal images of U87MG tumor-bearing mice after injection of magnetic AuNWs and PBS. The tumors were irradiated by an 808 nm CW laser at 0.75 W/cm^2. (d) Relative tumor volume and (e) survival curves of treatment group and all other control groups.

signals in tumor than that in muscle should be attributed to higher GSH level in tumor microenvironment than normal tissues.[33] Then these MRI contrast agents were administrated through intravenous injection to evaluate their T_1-weighted MR imaging functions. The results demonstrated that the brightest T_1-weighted tumor imaging for Magnevist or ES-MIONs respectively occurred at 1 or 4 h postinjection with 1.8 or 1.7 times of signal enhancement (Figure 4a,b,d,e). The brightest T_1-weighted tumor imaging by our magnetic AuNWs was found at 24 h postinjection with 2.5 times signal enhancement (Figure 4c,f). The brighter T_1-weighted images of our magnetic AuNWs in the tumor can be attributed to their higher accumulation in tumors compared with ES-MIONs and Magnevist and their activatable T_1 signal by interacting with GSH in the tumor microenvironment. Neither Magnevist nor ES-MIONs reached filtration-size threshold for renal clearance (∼6 nm), thus showing less retention in blood and faster clearance via kidney than the magnetic AuNWs.[28] In addition, ES-MIONs of such small size could diffuse from tumors back into blood vessels

more easily than larger magnetic AuNWs, leading to their shorter tumor retention time.[44] The concentration of Fe in tumors and kidneys were quantified by ICP at 24 h postinjection. A higher concentration of Fe in tumors and a lower concentration of Fe in kidneys after injection of magnetic AuNWs were obtained by compared to the corresponding concentrations of Fe in animals after injection of ES-MIONs (SI, Figure S16). These results were in consistent with the T_1-weighted tumor imaging results and supported our claim for the faster renal clearance of ES-MIONs. The GSH in tumor was sufficient to cleave the disulfide bonds in our magnetic AuNWs to release the individual ES-MIONs and turn on the T_1 signal. Therefore, magnetic AuNWs showed stronger T_1-weighted signal enhancement in tumor than ES-MIONs and Magnevist at later time points postinjection.

***In Vivo* Photoacoustic Imaging and Photothermal Therapy with the Magnetic AuNWs.** We evaluated the applications of the NIR-absorbing magnetic AuNWs in photoacoustic imaging and photothermal therapy. After intravenous

injections of the magnetic AuNWs, the tumors were irradiated by an 808 nm pulsed laser at different time points and the obtained ultrasonic emission was converted into imaging signal. Same as the MRI results, the photoacoustic imaging signals in tumors reached the highest at 24 h post injection, which was 5 times the background signal (Figure 5a,b). With the support of both imaging results, the best time point for conducting photothermal therapy was determined to be at 24 h post-injection. To evaluate the *in vivo* photothermal therapy with the magnetic AuNWs, U87MG tumor-bearing mice were divided into four groups by injecting PBS or magnetic AuNWs with or without laser irradiation of tumors. Compared to the PBS group, tumor areas of mice with magnetic AuNWs intravenously injected showed a significantly higher temperature after being exposed to laser irradiation for 5 min (Figure 5c and SI, Figure S17a). As a result, effective elimination of tumors was achieved in group of mice with systemic administration of the magnetic AuNWs followed by laser irradiation of tumors (Figure 5d). Lower survival rate was observed in other control groups due to the fast growth of tumors (Figure 5e). No significant difference in body weight was observed from each group, indicating the relatively low cytotoxicity of the magnetic AuNWs (SI, Figure S17b).

CONCLUSION

We synthesized a "smart" theranostic nanoplatform, magnetic AuNWs, via the combination of wet-chemical synthesis and layer-by-layer self-assembly. Of this nanoplatform, the core is made from AuNWs, which provides excellent photothermal property, and the shell is made from assembled ES-MIONs, which can be disassembled by responding to GSH. The assembly of ES-MIONs into bigger nanoparticles not only enhanced their tumor accumulation by inhibiting their fast-renal clearance but also generated GSH-responsive T_1 signal in tumor micro-environment. In addition to the bright T_1 imaging, the magnetic AuNWs can also greatly enhance the photoacoustic imaging contrast in tumor, which help to determine the best time point to conduct photothermal therapy. Finally, we demonstrated the effectiveness of our magnetic AuNWs in imaging-guided photo ablation of tumors. This work demonstrated that incorporation of stimuli-responsiveness into nanomaterials could improve their performance in biomedical applications and would provide more inspiration for the design of smart nanomaterials in the future.

METHODS

Preparation of Au Nanoring Seeds. The Au nanorings were prepared from a reported template method with minor modifications.[18] The initial templates, Ag nanoplates, were prepared from a seeded-mediated method. First, Ag seeds were prepared by adding sodium citrate (4.5×10^{-3} M), silver nitrate ($AgNO_3$) (1×10^{-4} M), hydrogen peroxide (480 μL), and sodium borohydride (6×10^{-4} M) into 200 mL of water with fast stirring. After purification with centrifugation, the Ag seeds were concentrated to 1 mL. Then Ag nanoplates of about 40 nm were prepared by introducing Ag seeds into an aqueous solution containing 3.4×10^{-4} M ascorbic acid (AA), 1.7×10^{-4} M sodium citrate, followed by adding $AgNO_3$ (1.7×10^{-4} M). Then a thin layer of Au was deposited on the edges of Ag nanoplates by injecting aqueous solutions of hydrogen tetrachloroaurate(III) trihydrate ($HAuCl_4$·$3H_2O$) and basic hydroxylamine hydrochloride into the aqueous dispersion of Ag nanoplates through two syringe pumps. The thin Au nanorings can be made after etching of Ag nanoplate templates from the Au-deposited Ag nanoplates by bis(*p*-sulfonatophenyl)phenylphosphine dihydrate dipotassium. Then, Au nanoring seeds were made by introducing $HAuCl_4$·$3H_2O$ and basic hydroxylamine hydrochloride to above

aqueous dispersion of thin Au nanorings until the absorption peak shifted to 1100 nm. The Au nanoring seeds were purified by centrifugation to remove the excess ligands and other impurities and dissolved in water for further use.

Preparation of AuNWs. Au nanoring seeds were dissolved in 2 mL of water with 350 μL of $HAuCl_4$·$3H_2O$ (1 wt ‰). Then 50 μL of 3 mM $AgNO_3$ (aq) and 25 μL of 100 mM AA (aq) were injected to the above solution at the same time with rapid stirring. Immediately, the solution color turned to blue, indicating the completion of the reaction. AuNWs with larger size and longer branches can be produced by increasing the ratio of $HAuCl_4$·$3H_2O$ to Au nanoring seeds.

Preparation of AuNWs@SiO_2. First, 1 mL of 1 mg/mL thiol-terminated polyethylene glycol (SH-PEG) (MW 5k) was added to above aqueous dispersion of AuNWs. Then PEG stabilized AuNWs were centrifuged at 6500 rpm to remove the excess polymer ligands and were dispersed into 2.5 mL of water. The aqueous solution of PEG stabilized AuNWs was mixed with 6 mL of 2-propanol, followed by adding 150 μL of 1% TEOS in ethanol and 200 μL of ammonium solution (28%) with stirring. The reaction was stirred for 8 h before purification by centrifugation.

Preparation of ES-MIONs. The ES-MIONs were prepared via a reported method.[28,27] Briefly, 80 mg PAA ($M_w = 1800$) was dissolved in 20 mL of water and was purged with nitrogen ($\geq$50 min) for deoxygenation. Then the polymer solution was heated to reflux, into which a 0.4 mL aqueous solution containing 500 mM $FeCl_3$ and 250 mM $FeSO_4$ was quickly injected. Then 6.0 mL of ammonia solution (28%) was added. The polymer solution was kept at 100 °C under magnetic stirring for 1 h before the solutions were cooled down to room temperature. The obtained ES-MIONs were purified by dialyzing against water for 5 days (MW cutoff: 6−8 kDa).

Preparation of Mono-Boc-cystamine. First, 10 g of cystamine bis(dihydrochloride) was dissolved in 200 mL of dry methanol together with 13.5 g of triethylamine. Then a dry methanol solution of di-*tert*-butyldicarbonate (4.9 g) was added into the reaction dropwise over 40 min. The reaction mixture was stirred overnight. After evaporation of solvent, the solids were dissolved in an aqueous solution of mono-sodium phosphate with pH around 4.3 and undissolved impurities were removed by filtration. The pH of the solution was adjusted to 9.1 with addition of 1 M sodium hydroxide, and the resulting solution was extracted with ethyl acetate. The product was obtained after evaporation of the ethyl acetate.

Preparation of Mono-Boc-cystamine Methacrylamide. Mono-Boc-cystamine (2.4 g) was dissolved in 50 mL of chloroform followed by the addition of 4.2 mL of triethylamine. In this mixture, 2.4 g of methacryloyl chloride was added. The reaction was stirred at room temperature for 24 h. After evaporation of solvent, the dried powder was washed with sodium bicarbonate solution for several times for purification.

Preparation of Poly Boc-cystamine-*co*-polyoligo(ethylene glycol) Methyl Ether Methacrylate. 4-Cyano-4-(phenylcar-bonothioylthio)pentanoic acid (4.4 mg), 0.5 mg of 2,2′-azobis(2-methylpropionitrile), 500 mg of mono-Boc-cystamine methacrylamide, and 188 mg of poly(ethylene glycol) methyl ether methacrylate (MW 500) was dissolved in a mixture of 1 mL of dimethylformamide and 1.5 mL of dioxane in a sealed round-bottom flask equipped with a stir bar. The solution was deoxygenated by nitrogen gas purging for 30 min followed by being placed into an oil bath preheated at 75 °C for 24 h. After reaction was quenched by liquid nitrogen, the polymer was precipitated from the solution by cold ether. The polymer was dried in vacuum for further use. The repeating unit numbers for Boc-cystamine and oligo(ethylene glycol) methyl ether methacrylate were 25 and 7, respectively.

Preparation of Poly Cystamine-*co*-polyoligo(ethylene glycol) Methyl Ether Methacrylate. The poly Boc-cystamine-*co*-polyoligo(ethylene glycol) methyl ether methacrylate was dissolved in 3 mL of dichloromethane, into which 1 mL of trifluoroacetic acid was added. The reaction was stirred overnight. The polymer was precipitated by cold ether to remove impurities.

Self-Assembly of {Poly Cystamine-*co*-polyoligo(ethylene glycol) Methyl Ether Methacrylate on AuNWs@SiO_2. A 4 mL

aqueous solution the poly cystamine-*co*-polyoligo(ethylene glycol) methyl ether methacrylate was prepared (10 mg/mL), in which the prepared AuNWs@SiO$_2$ was added dropwise with sonication. The solution was stirred for 4 h before the polymer-coated AuNWs@SiO$_2$ was separated from free polymers by centrifugation for 3 times. The polymer-coated AuNWs@SiO$_2$ was finally dissolved in 25 μL of water.

Preparation of Magnetic AuNWs. ES-MIONs (0.8 mL, 16 mM) was concentrated by centricon and dissolved in 80 μL of acetic acid/sodium acetate buffer (10 mM pH 5.5) containing 80 mM NaCl. The above solution of AuNWs@SiO$_2$ was added into the dispersion of concentrated ES-MIONs with sonication. The solution mixture was kept shaking for 30 min before the free ES-MIONs were removed by centrifugation. The magnetic AuNWs were pegylated by reacting with amine-terminated PEG through EDC coupling.

ASSOCIATED CONTENT

Ⓢ Supporting Information

The Supporting Information is available free of charge on the ACS Publications website at DOI: 10.1021/acsnano.8b02980.

Experimental details, TEM and MRI images, and ^{1}H NMR spectra (PDF)

AUTHOR INFORMATION

Corresponding Authors
*X.C.: E-mail, shawn.chen@nih.gov.
*Z.S.: E-mail, shenzheyu@nimte.ac.cn.
*Z.N.: E-mail, znie@umd.edu.

ORCID Ⓘ
Zhen Yang: 0000-0003-4056-0347
Zhihong Nie: 0000-0001-9639-905X
Xiaoyuan Chen: 0000-0002-9622-0870

Notes
The authors declare no competing financial interest.

REFERENCES

(1) Matsumura, Y.; Maeda, H. A New Concept for Macromolecular Therapeutics In Cancer Chemotherapy: Mechanism of Tumoritropic Accumulation of Proteins and The Antitumor Agent Smancs. *Cancer Res.* **1986**, *46*, 6387−6382.

(2) Matsumoto, Y.; Nichols, J. W.; Toh, K.; Nomoto, T.; Cabral, H.; Miura, Y.; Christie, R. J.; Yamada, N.; Ogura, T.; Kano, M. R.; Matsumura, Y.; Nishiyama, N.; Yamasoba, T.; Bae, Y. H.; Kataoka, K. Vascular Bursts Enhance Permeability of Tumour Blood Vessels and Improve Nanoparticle Delivery. *Nat. Nanotechnol.* **2016**, *11*, 533−538.

(3) Setyawati, M. I.; Tay, C. Y.; Chia, S. L.; Goh, S. L.; Fang, W.; Neo, M. J.; Chong, H. C.; Tan, S. M.; Loo, S. C. J.; Ng, K. W.; Xie, J. P.; Ong, C. N.; Tan, N. S.; Leong, D. T. Titanium Dioxide Nanomaterials Cause Endothelial Cell Leakiness By Disrupting The Homophilic Interaction of VE-Cadherin. *Nat. Commun.* **2013**, *4*, 1673.

(4) Tavares, A. J.; Poon, W.; Zhang, Y.-N.; Dai, Q.; Besla, R.; Ding, D.; Ouyang, B.; Li, A.; Chen, J.; Zheng, G.; Robbins, C.; Chan, W. C. W. Effect of Removing Kupffer Cells on Nanoparticle Tumor Delivery. *Proc. Natl. Acad. Sci. U. S. A.* **2017**, *114*, E10871−E10880.

(5) Zhao, T.; Wang, P.; Li, Q.; Al-Khalaf, A. A.; Hozzein, W. N.; Zhang, F.; Li, X.; Zhao, D. Near-Infrared Triggered Decomposition of Nanocapsules with High Tumor Accumulation and Stimuli Responsive Fast Elimination. *Angew. Chem.* **2018**, *130*, 2641−2645.

(6) Sánchez-Iglesias, A.; Claes, N.; Solís, D. M.; Taboada, J. M.; Bals, S.; Liz-Marzán, L. M.; Grzelczak, M. Reversible Clustering of Gold Nanoparticles under Confinement. *Angew. Chem.* **2018**, *130*, 3237−3240.

(7) Yang, Y.; Lu, Y.; Abbaraju, P. L.; Zhang, J.; Zhang, M.; Xiang, G.; Yu, C. Multi-shelled Dendritic Mesoporous Organosilica Hollow Spheres: Roles of Composition and Architecture in Cancer Immunotherapy. *Angew. Chem.* **2017**, *129*, 8566−8570.

(8) González-Rubio, G.; Díaz-Núñez, P.; Rivera, A.; Prada, A.; Tardajos, G.; González-Izquierdo, J.; Bañares, L.; Llombart, P.; Macdowell, L. G.; Alcolea Palafox, M.; Liz-Marzán, L. M.; Peña-Rodríguez, O.; Guerrero-Martínez, A. Femtosecond Laser Reshaping Yields Gold Nanorods With Ultranarrow Surface Plasmon Resonances. *Science* **2017**, *358* (6363), 640−644.

(9) Zhou, J.; Jiang, Y.; Hou, S.; Upputuri, P. K.; Wu, D.; Li, J.; Wang, P.; Zhen, X.; Pramanik, M.; Pu, K.; Duan, H. Compact Plasmonic Blackbody for Cancer Theranosis in the Near-Infrared II Window. *ACS Nano* **2018**, *12*, 2643−2651.

(10) Gilroy, K. D.; Peng, H.-C.; Yang, X.; Ruditskiy, A.; Xia, Y. Symmetry Breaking During Nanocrystal Growth. *Chem. Commun.* **2017**, *53*, 4530−4541.

(11) Huang, L.; Chen, P.-C.; Liu, M.; Fu, X.; Gordiichuk, P.; Yu, Y.; Wolverton, C.; Kang, Y.; Mirkin, C. A. Catalyst Design By Scanning Probe Block Copolymer Lithography. *Proc. Natl. Acad. Sci. U. S. A.* **2018**, *115*, 3764−3769.

(12) Huang, Z.; Liu, Y.; Zhang, Q.; Chang, X.; Li, A.; Deng, L.; Yi, C.; Yang, Y.; Khashab, N. M.; Gong, J.; Nie, Z. Collapsed Polymer-Directed Synthesis of Multicomponent Coaxial-Like Nanostructures. *Nat. Commun.* **2016**, *7*, 12147.

(13) Chen, H.; Zhang, W.; Zhu, G.; Xie, J.; Chen, X. Rethinking Cancer Nanotheranostics. *Nat. Rev. Mater.* **2017**, *2*, 17024.

(14) Blanco, E.; Shen, H.; Ferrari, M. Principles of Nanoparticle Design for Overcoming Biological Barriers to Drug Delivery. *Nat. Biotechnol.* **2015**, *33*, 941−951.

(15) Tang, L.; Yang, X.; Yin, Q.; Cai, K.; Wang, H.; Chaudhury, I.; Yao, C.; Zhou, Q.; Kwon, M.; Hartman, J. A.; Dobrucki, I. T.; Dobrucki, L. W.; Borst, L. B.; Lezmi, S.; Helferich, W. G.; Ferguson, A. L.; Fan, T. M.; Cheng, J. Investigating the Optimal Size of Anticancer Nanomedicine. *Proc. Natl. Acad. Sci. U. S. A.* **2014**, *111*, 15344−15349.

(16) Sykes, E. A.; Chen, J.; Zheng, G.; Chan, W. C. W. Investigating the Impact of Nanoparticle Size on Active And Passive Tumor Targeting Efficiency. *ACS Nano* **2014**, *8* (6), 5696−5706.

(17) Du, B.; Jiang, X.; Das, A.; Zhou, Q.; Yu, M.; Jin, R.; Zheng, J. Glomerular Barrier Behaves as An Atomically Precise Bandpass Filter in A Sub-Nanometre Regime. *Nat. Nanotechnol.* **2017**, *12*, 1096.

(18) Liu, Y.; Wang, Z.; Liu, Y.; Zhu, G.; Jacobson, O.; Fu, X.; Bai, R.; Lin, X.; Lu, N.; Yang, X.; Fan, W.; Song, J.; Wang, Z.; Yu, G.; Zhang, F.; Kalish, H.; Niu, G.; Nie, Z.; Chen, X. Suppressing Nanoparticle-Mononuclear Phagocyte System Interactions of Two-Dimensional Gold Nanorings for Improved Tumor Accumulation and Photothermal Ablation of Tumors. *ACS Nano* **2017**, *11*, 10539−10548.

(19) Zhen, X.; Zhang, C.; Xie, C.; Miao, Q.; Lim, K. L.; Pu, K. Intraparticle Energy Level Alignment of Semiconducting Polymer Nanoparticles to Amplify Chemiluminescence for Ultrasensitive In Vivo Imaging of Reactive Oxygen Species. *ACS Nano* **2016**, *10*, 6400−6409.

(20) Ali, M. R. K.; Wu, Y.; Tang, Y.; Xiao, H.; Chen, K.; Han, T.; Fang, N.; Wu, R.; El-Sayed, M. A. Targeting Cancer Cell Integrins Using Gold Nanorods in Photothermal Therapy Inhibits Migration Through Affecting Cytoskeletal Proteins. *Proc. Natl. Acad. Sci. U. S. A.* **2017**, *114*, E5655−E5663.

(21) Abadeer, N. S.; Murphy, C. J. Recent Progress in Cancer Thermal Therapy Using Gold Nanoparticles. *J. Phys. Chem. C* **2016**, *120*, 4691−4716.

(22) Jiang, N.; Zhuo, X.; Wang, J. Active Plasmonics: Principles, Structures, and Applications. *Chem. Rev.* **2018**, *118* (6), 3054−3099.

(23) Liu, Y.; He, J.; Yang, K.; Yi, C.; Liu, Y.; Nie, L.; Khashab, N. M.; Chen, X.; Nie, Z. Folding Up of Gold Nanoparticle Strings into Plasmonic Vesicles for Enhanced Photoacoustic Imaging. *Angew. Chem., Int. Ed.* **2015**, *54*, 15809−15812.

(24) Wang, S.; Lin, J.; Wang, T. F.; Chen, X. Y.; Huang, P. Recent Advances in Photoacoustic Imaging for Deep-Tissue Biomedical Applications. *Theranostics* **2016**, *6*, 2394−2413.

(25) Zhen, X.; Xie, C.; Pu, K. Temperature-Correlated Afterglow of a Semiconducting Polymer Nanococktail for Imaging-Guided Photothermal Therapy. *Angew. Chem.* **2018**, *130*, 4002−4006.

(26) Ni, D.; Bu, W.; Ehlerding, E. B.; Cai, W.; Shi, J. Engineering of Inorganic Nanoparticles as Magnetic Resonance Imaging Contrast Agents. *Chem. Soc. Rev.* **2017**, *46*, 7438−7468.

(27) Shen, Z.; Wu, A.; Chen, X. Iron Oxide Nanoparticle Based Contrast Agents for Magnetic Resonance Imaging. *Mol. Pharmaceutics* **2017**, *14*, 1352−1364.

(28) Shen, Z.; Chen, T.; Ma, X.; Ren, W.; Zhou, Z.; Zhu, G.; Zhang, A.; Liu, Y.; Song, J.; Li, Z.; Ruan, H.; Fan, W.; Lin, L.; Munasinghe, J.; Chen, X.; Wu, A. Multifunctional Theranostic Nanoparticles Based on Exceedingly Small Magnetic Iron Oxide Nanoparticles for T_1-Weighted Magnetic Resonance Imaging and Chemotherapy. *ACS Nano* **2017**, *11*, 10992−11004.

(29) Lu, Y.; Xu, Y.-J.; Zhang, G.-b.; Ling, D.; Wang, M.-q.; Zhou, Y.; Wu, Y.-D.; Wu, T.; Hackett, M. J.; Hyo Kim, B.; Chang, H.; Kim, J.; Hu, X.-T.; Dong, L.; Lee, N.; Li, F.; He, J.-C.; Zhang, L.; Wen, H.-Q.; Yang, B.; Hong Choi, S.; Hyeon, T.; Zou, D.-H. Iron oxide nanoclusters for T_1 magnetic resonance imaging of non-human primates. *Nature Biomedical Engineering* **2017**, *1*, 637−643.

(30) Penfield, J. G.; Reilly, R. F., Jr What Nephrologists Need to Know About Gadolinium. *Nat. Clin. Pract. Nephrol.* **2007**, *3*, 654.

(31) Ling, D.; Park, W.; Park, S.-j.; Lu, Y.; Kim, K. S.; Hackett, M. J.; Kim, B. H.; Yim, H.; Jeon, Y. S.; Na, K.; Hyeon, T. Multifunctional Tumor pH-Sensitive Self-Assembled Nanoparticles for Bimodal Imaging and Treatment of Resistant Heterogeneous Tumors. *J. Am. Chem. Soc.* **2014**, *136*, 5647−5655.

(32) Zhou, H.; Tang, J.; Li, J.; Li, W.; Liu, Y.; Chen, C. *In vivo* Aggregation-Induced Transition Between T_1 And T_2 Relaxations of Magnetic Ultra-Small Iron Oxide Nanoparticles in Tumor Microenvironment. *Nanoscale* **2017**, *9*, 3040−3050.

(33) Kuppusamy, P.; Li, H.; Ilangovan, G.; Cardounel, A. J.; Zweier, J. L.; Yamada, K.; Krishna, M. C.; Mitchell, J. B. Noninvasive Imaging of Tumor Redox Status and Its Modification by Tissue Glutathione Levels. *Cancer Res.* **2002**, *62*, 307−312.

(34) Gao, Z.; Hou, Y.; Zeng, J.; Chen, L.; Liu, C.; Yang, W.; Gao, M. Tumor Microenvironment-Triggered Aggregation of Antiphagocytosis ^{99}mTc-Labeled Fe_3O_4 Nanoprobes for Enhanced Tumor Imaging *In vivo*. *Adv. Mater.* **2017**, *29*, 1701095.

(35) Zhao, Z.; Fan, H.; Zhou, G.; Bai, H.; Liang, H.; Wang, R.; Zhang, X.; Tan, W. Activatable Fluorescence/MRI Bimodal Platform for Tumor Cell Imaging *via* MnO_2 Nanosheet−Aptamer Nanoprobe. *J. Am. Chem. Soc.* **2014**, *136*, 11220−11223.

(36) Jiang, Y.; Li, J.; Zhen, X.; Xie, C.; Pu, K. Dual-Peak Absorbing Semiconducting Copolymer Nanoparticles for First and Second Near-Infrared Window Photothermal Therapy: A Comparative Study. *Adv. Mater.* **2018**, *30*, 1705980.

(37) Li, J.; Xie, C.; Huang, J.; Jiang, Y.; Miao, Q.; Pu, K. Semiconducting Polymer Nanoenzymes with Photothermic Activity for Enhanced Cancer Therapy. *Angew. Chem., Int. Ed.* **2018**, *57*, 3995−3998.

(38) Lyu, Y.; Zeng, J.; Jiang, Y.; Zhen, X.; Wang, T.; Qiu, S.; Lou, X.; Gao, M.; Pu, K. Enhancing Both Biodegradability and Efficacy of Semiconducting Polymer Nanoparticles for Photoacoustic Imaging and Photothermal Therapy. *ACS Nano* **2018**, *12*, 1801−1810.

(39) Melancon, M. P.; Zhou, M.; Li, C. Cancer Theranostics with Near-Infrared Light-Activatable Multimodal Nanoparticles. *Acc. Chem. Res.* **2011**, *44*, 947−956.

(40) Tang, Z.; Zhang, H.; Liu, Y.; Ni, D.; Zhang, H.; Zhang, J.; Yao, Z.; He, M.; Shi, J.; Bu, W. Antiferromagnetic Pyrite as the Tumor Microenvironment-Mediated Nanoplatform for Self-Enhanced Tumor Imaging and Therapy. *Adv. Mater.* **2017**, *29*, 1701683.

(41) Ni, D.; Zhang, J.; Wang, J.; Hu, P.; Jin, Y.; Tang, Z.; Yao, Z.; Bu, W.; Shi, J. Oxygen Vacancy Enables Markedly Enhanced Magnetic Resonance Imaging-Guided Photothermal Therapy of a Gd^{3+}-Doped Contrast Agent. *ACS Nano* **2017**, *11*, 4256−4264.

(42) Zhou, Z.; Tian, R.; Wang, Z.; Yang, Z.; Liu, Y.; Liu, G.; Wang, R.; Gao, J.; Song, J.; Nie, L.; Chen, X. Artificial Local Magnetic Field Inhomogeneity Enhances T_2 Relaxivity. *Nat. Commun.* **2017**, *8*, 15468.

(43) Zhou, Z.; Bai, R.; Munasinghe, J.; Shen, Z.; Nie, L.; Chen, X. T1−T2 Dual-Modal Magnetic Resonance Imaging: From Molecular Basis to Contrast Agents. *ACS Nano* **2017**, *11*, 5227−5232.

(44) Wang, L.; Huang, J.; Chen, H.; Wu, H.; Xu, Y.; Li, Y.; Yi, H.; Wang, Y. A.; Yang, L.; Mao, H. Exerting Enhanced Permeability and Retention Effect Driven Delivery by Ultrafine Iron Oxide Nanoparticles with $T_1−T_2$ Switchable Magnetic Resonance Imaging Contrast. *ACS Nano* **2017**, *11*, 4582−4592.